Segmented simultaneous multi-slice diffusion-weighted imaging with navigated 3D rigid motion correction

Riedel, M.; Setsompop, K.; Mertins, A.; Bornert, P.

Received: 2 November 2020 | Revised: 29 March 2021 | Accepted: 29 March 2021

DOI: 10.1002/mrm.28813

FULL PAPER

Magnetic Resonance in Medicine

Segmented simultaneous multi-slice diffusion-weighted imaging with navigated 3D rigid motion correction

Malte Riedel (né Steinhoff)[1] | **Kawin Setsompop**[2,3,4] | **Alfred Mertins**[1] | **Peter Börnert**[5,6]

[1]Institute for Signal Processing, University of Luebeck, Luebeck, Germany

[2]Athinoula A. Martinos Center for Biomedical Imaging, Charlestown, Massachusetts, USA

[3]Department of Radiology, Harvard Medical School, Boston, Massachusetts, USA

[4]Harvard-MIT Health Sciences and Technology, MIT, Cambridge, Massachusetts, USA

[5]Philips Research, Hamburg, Germany

[6]Radiology, C.J. Gorter Center for High-Field MRI, Leiden University Medical Center, Leiden, The Netherlands

Correspondence
Malte Riedel, Institute for Signal Processing, University of Luebeck, Ratzeburger Allee 160, 23562 Luebeck, Germany.
Email: mr-riedel@gmx.de

Funding information
Philips

Purpose: To improve the robustness of diffusion-weighted imaging (DWI) data acquired with segmented simultaneous multi-slice (SMS) echo-planar imaging (EPI) against in-plane and through-plane rigid motion.

Theory and Methods: The proposed algorithm incorporates a 3D rigid motion correction and wavelet denoising into the image reconstruction of segmented SMS-EPI diffusion data. Low-resolution navigators are used to estimate shot-specific diffusion phase corruptions and 3D rigid motion parameters through SMS-to-volume registration. The shot-wise rigid motion and phase parameters are integrated into a SENSE-based full-volume reconstruction for each diffusion direction. The algorithm is compared to a navigated SMS reconstruction without gross motion correction in simulations and in vivo studies with four-fold interleaved 3-SMS diffusion tensor acquisitions.

Results: Simulations demonstrate high fidelity was achieved in the SMS-to-volume registration, with submillimeter registration errors and improved image reconstruction quality. In vivo experiments validate successful artifact reduction in 3D motion-compromised in vivo scans with a temporal motion resolution of approximately 0.3 s.

Conclusion: This work demonstrates the feasibility of retrospective 3D rigid motion correction from shot navigators for segmented SMS DWI.

KEYWORDS

brain, EPI, full-volume reconstruction, model-based image reconstruction, motion correction, multi-shot DWI

1 | INTRODUCTION

Diffusion-weighted imaging (DWI) is a key contrast in both diagnostic imaging and neurological applications.[1,2] Strong diffusion gradients encode diffusion information on the scale of 10 microns,[1] but make the sequence also susceptible to various types of patient motion.[2] Model-based image reconstructions[3] can help alleviate the trade-offs between scan design and motion sensitivity by properly modeling the signal variations over time.

Single-shot echo-planar imaging (EPI) has for years been the clinical standard for DWI, as it suppresses motion artifacts by fast one-time k-space traversal[2] being commonly accelerated by parallel imaging[4] using SENSE[5,6] or GRAPPA.[7] Multi-shot techniques[8] have been developed to mitigate the shortcomings of single-shot EPI, such as limited resolution and susceptibility to geometric distortions, but come at the cost of further sensitivity to shot-to-shot variations. Model-based reconstructions are usually classified according to the signal that is used to sense the shot-to-shot variations. *Navigated* methods acquire additional MR signals for this purpose, while *extra-navigated* methods use external sensor signals. *Self-navigated* methods derive navigation signals from the imaging data itself and *navigator-free* methods yield problem formulations that do not require explicit navigation.

Most prominently, cardiac pulsation and tiny patient motion during the diffusion encoding introduce severe shot-to-shot phase variations.[9,10] Multi-shot DWI with shot-specific phase corrections initially used MR navigators,[9-16] which have been complemented by effective self-navigated[17-21] and navigator-free[22,23] methods. The *navigated* IRIS algorithm,[16] in particular, uses 2D low-resolution navigators from a second spin echo to sense the shot-to-shot phase variations and integrates them into an efficient SENSE-based[5] image-space algorithm. In addition to the phase variations, the lengthy scans are prone to macroscopic motion between the shots[24] that can be corrected using dedicated motion modeling.[25-28] For brain DWI, this has been addressed by *retrospective rigid in-plane* corrections using navigators,[29,30] self-navigation[31,32] as well as *prospective 3D rigid* corrections using image-based navigation[33] or camera-based extra-navigation.[34-37] Moreover, multi-shot DWI datasets are commonly analyzed using dedicated shot criteria to reject,[11,12] reweight,[13,17] or even reacquire[15] heavily corrupted signals.

In addition to the in-plane accelerations through segmentation/multi-shot, simultaneous multi-slice[38] (SMS) approaches offer scan time reductions without an immediate loss of signal-to-noise ratio (SNR). Controlled aliasing in parallel imaging (CAIPI) techniques[39,40] improved the coil encoding efficiency and were successfully combined with EPI by blipped-CAIPI[41] and SENSE.[42,43] Combining SMS and segmented DWI, several algorithms have been proposed for shot-to-shot phase corrections with navigated,[44] self-navigated,[45,46] and navigator-free[47] approaches. Further macroscopic motion corrections have been developed using external tracking devices and intermediate non-diffusion-weighted navigators.[48] Recent approaches exploit SMS acceleration for single-shot EPI to obtain signal support in the slice direction and propose SMS-to-volume registration for 3D rigid motion-corrected fMRI[49,50] and diffusion tensor fitting.[51]

In this work, we extend the navigated IRIS approach for segmented DWI[16] with SMS[44] and investigate the potential of 3D rigid motion-corrected DWI reconstructions. The proposed algorithm, termed motion-aware SMS-accelerated and interleaved image creation (MoSaIC) for DWI, estimates shot-specific phase maps and 3D rigid motion from low-resolution SMS navigators and reconstructs motion-corrected DWI volumes per diffusion direction. We further implemented an SMS extension for the IRIS[16] algorithm, termed SMS-IRIS, as a phase-navigated reference algorithm without rigid motion correction.

2 | THEORY

2.1 | Segmented SMS DWI sampling

The proposed method is based on a navigated Stejskal-Tanner spin-echo sequence for DWI.[16] The first spin echo samples the interleaved high-resolution *image echo*, while a second spin echo acquires a low-resolution *navigator echo* at a lower undersampling rate. The echo-spacings are adjusted to match the off-resonance-induced distortions in phase encoding direction for both samplings. The navigated DWI sequence is extended to SMS and blipped-CAIPI encoding as described by Dai et al.[44] The pulse sequence is visualized in Supporting Information Figure S1, which is available online.

The reconstruction problem for segmented SMS DWI under shot-to-shot phase variations und macroscopic inter-shot motion is summarized in Figure 1. The high-resolution images of one SMS slice group for two interleaves in Figure 1B were produced from an in vivo case using the motion-informed forward model. The shot-specific phase and macroscopic motion variations cause severe ghosting and blurring for the motion-unaware 2D-SENSE[43] in Figure 1C. The MoSaIC algorithm corrects for the shot-to-shot phase variations and 3D rigid motion.

2.2 | Model formulation for 3D motion corrected DWI

The model extension to address through-plane motion requires a full-volume reconstruction framework as used in Ref. 28, rather than the standard slice-by-slice reconstruction.

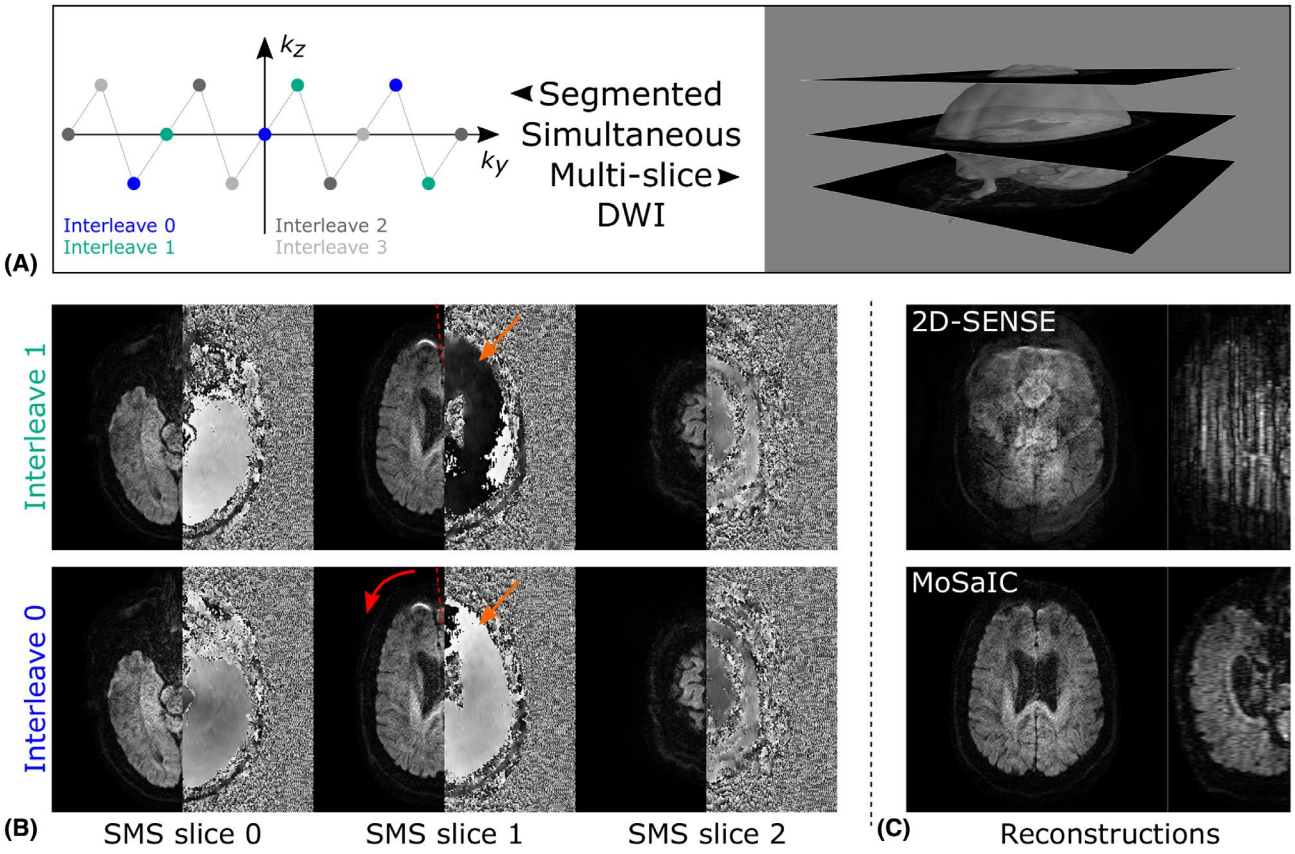

FIGURE 1 Segmented SMS DWI sampling and reconstruction problem for a four-fold interleaved 3-SMS DWI acquisition. A, This example visualizes the segmented SMS sampling. The variations of two interleaves from the same SMS slice group are shown (please note that here magnitude and phase are illustrated for each dataset) (B), along with two SENSE-based reconstructions (C). The two interleaves contain diffusion-related physiology-induced phase variations (orange arrows) causing ghosting and signal dropouts in a CAIPI-adapted 2D-SENSE reconstruction. Second, macroscopic motion, here in-plane, (red arrow) is a common problem, which blurs anatomical structures. Moreover, through-plane motion mixes the anatomies of different slice groups. MoSaIC is a navigated technique that produces full volume reconstructions per diffusion direction with 3D rigid motion and physiological phase correction. (C) This can be seen for the transversal example slice as well at the coronal reformat next to it

The slice positions of an SMS stack in the scanner frame are in the first place determined by the slice gradients and the RF excitation, independent of subject motion. For pure in-plane motion, the anatomies therefore stay in the same SMS stack as long as the object remains within the field of view (FOV). For through-plane motion, new anatomies enter the slice positions decoupling the strict assignment of anatomies to SMS slice stacks so that a full-volume reconstruction is required to resolve the motion. The model furthermore assumes that the signal encoding remains unchanged in the scanner frame and is explicitly unaffected by macroscopic subject motion. Thus, the spatial profiles of the coil sensitivities stay valid during the whole scan and continuously weight the new anatomies entering the imaged slice stack.

To facilitate the model description, some notations are given here in advance. N_x, N_y and N_z are the number of voxels in readout, phase, and slice encoding direction, respectively, giving in total $N_\rho = N_x N_y N_z$ voxels. The volume is sampled with N_c coils, N_{MB} simultaneously acquired slices and N_i interleaves. A full volume is covered by $N_g = N_z/N_{MB}$ SMS slice group excitations. Each of the N_d diffusion directions is thus sampled by $N_{shots} = N_i N_g$ shots. For fully interleaved sampling, the number of samples is $N_b = N_c N_{shots} \left(N_y/R_P\right) N_x$ with an effective shot reduction of $R_P = N_i$ in phase encoding direction.

The individual shot operators of the forward model are visualized in Figure 2. The individual (and parallelizable) shot operators are stacked in block-diagonal structure into the following multi-shot operators. Based on the formulated assumptions, the forward model relates the multi-shot and multi-coil data $\boldsymbol{b} \in \mathbb{C}^{N_b}$ to the image volume $\boldsymbol{\rho} \in \mathbb{C}^{N_\rho}$ by several linear operators and a complex Gaussian white noise vector $\boldsymbol{\eta} \in \mathbb{C}^{N_b}$:

$$\boldsymbol{b} = M^{trj} F \Theta C \Phi M^{sms} \Omega \boldsymbol{\rho} + \boldsymbol{\eta}. \tag{1}$$

First, the macroscopic motion operator Ω $(N_{shots} N_z N_y N_x \times N_z N_y N_x)$ resamples the image

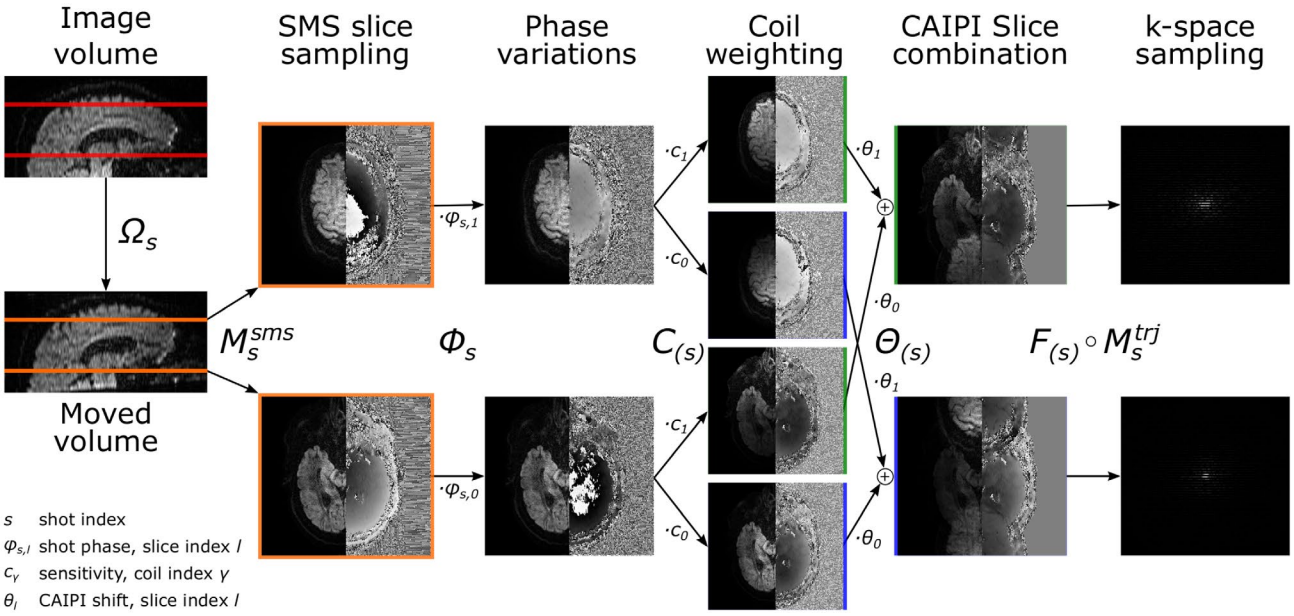

FIGURE 2 Illustration of the shot-specific forward model employed for motion-corrected segmented SMS DWI (using a SMS factor of 2). The image volume is resampled by the macroscopic motion operator Ω_s according to the motion transformation of shot s. The slice-sampling operator M_s^{sms} selects the shot-specific slices. The signal is weighted by the diffusion shot phases and coil sensitivities in Φ_s and $C_{(s)}$. $\Theta_{(s)}$ applies the blipped-CAIPI encoding and slice combination followed by the Fourier operator $F_{(s)}$ and shot-specific trajectory sampling M_s^{trj}. The subscript (s) with shot index s in parentheses indicates shot operators that are equal for all shots. The multi-shot operators (Equation 1) are obtained by embedding the shot operators in block-diagonal structure

volume according to the macroscopic shot motion parameters. Second, the slice-sampling operator M^{sms} $(N_{shots}N_{MB}N_yN_x \times N_{shots}N_zN_yN_x)$ selects the SMS slices excited for each shot. Third, the physiological motion operator Φ $(N_{shots}N_{MB}N_yN_x \times N_{shots}N_{MB}N_yN_x)$ applies the shot- and slice-specific phase variations, followed by the coil weighting of the sensitivity operator C $(N_cN_{shots}N_{MB}N_yN_x \times N_{shots}N_{MB}N_yN_x)$. Fifth, the CAIPI operator Θ $(N_cN_{shots}N_yN_x \times N_cN_{shots}N_{MB}N_yN_x)$ combines the SMS slices including CAIPI shifts. Finally, the coil images are Fourier transformed by F to sample the shot-specific trajectories using M^{trj} $(N_cN_{shots}\left(N_y/R_P\right)N_x \times N_cN_{shots}N_yN_x)$.

2.3 | Model-based image reconstruction

The optimization problem for motion-corrected segmented SMS DWI is stated as a regularized data discrepancy minimization:

$$\underset{\boldsymbol{\rho},\Phi,\Omega}{\text{minimize}} \left\| M^{trj}F\Theta C\Phi M^{sms}\Omega\boldsymbol{\rho} - b \right\|_{\Psi^{-1}}^2 + \alpha R(\boldsymbol{\rho}), \quad (2)$$

where the weighted norm $\|\cdot\|_{\Psi^{-1}}^2 = (\cdot)^H \Psi^{-1} (\cdot)$ integrates the noise covariance matrix Ψ for SNR-optimal reconstruction as used for SENSE.[5] R is a regularization function and α a weighting factor. The proposed MoSaIC algorithm employs an $\ell 1$-norm regularization $R(\boldsymbol{\rho}) = \|T\boldsymbol{\rho}\|_1$ in a wavelet domain[52] with transform operator T $(N_\rho \times N_\rho)$. The image volume $\boldsymbol{\rho}$, the shot phase operator Φ and the macroscopic motion operator Ω are considered unknown. The problem is difficult to optimize due to the non-convexity associated with both Ω and Φ.

Navigation approaches are used to linearize and simplify the nonconvex optimization by estimating reconstruction parameters from an additional signal.[16,29,44] The proposed method leverages the low-resolution navigator echo to estimate the shot phase operator Φ and the macroscopic motion operator Ω. For known Φ and Ω, Equation (2) with $\ell 1$-norm regularization represents a convex optimization problem for $\boldsymbol{\rho}$, which can be readily solved using fast gradient projections (FGP).[53]

3 | METHODS

3.1 | Data acquisition and preprocessing

DTI data were acquired using a navigated Stejskal-Tanner spin-echo sequence with blipped-CAIPI[41] SMS excitation similar to the work by Dai et al.[44] Unlike this publication, the prewinder phase offset φ_{offset}[44] was implemented as originally proposed,[41] as for this SENSE implementation the samples are not required to lie on an integer-valued k-space grid. Thus, the k_z-sampling is centered around zero by $\varphi_{\text{offset}} = -\frac{(D-1)}{2}\frac{2\pi}{D}, D \in \mathbb{N}$ for a FOV_y/D CAIPI shift between two adjacent SMS slices. The first image echo was

sampled at high-resolution in an interleaved fashion with a CAIPI shift of FOV_y/N_{MB} ($D_1 = N_{MB}$). The second echo used a moderately accelerated low-resolution sampling with a fixed CAIPI shift of $FOV_y/2$ ($D_2 = 2$). The navigator CAIPI shift was fixed for simplicity reasons. Given the z-encoding capabilities of the used 32-channel coil, the CAIPI encoding showed sufficient slice disentangling capabilities. The SMS slice groups were sampled in an interleaved ordering to reduce slice crosstalk.[38] Fat suppression was performed by spectral pre-saturation with inversion recovery. The SMS slices were excited with slice-specific radiofrequency (RF) phases to reduce the peak B1.[38] Further sampling parameters are listed in Table 1.

The data were acquired on a 3T Philips Ingenia Scanner (Best, The Netherlands) using a 32-channel head coil. The scan session was carried out on five healthy volunteers. Informed consent was attained according to the rules of the institution. The DTI scan with 15 diffusion directions was performed twice under different motion conditions:

1. Static: no voluntary motion
2. Motion: separated into four parts:
   a. T_2-weighted images no voluntary motion (for b = 0 s/mm^2 data)
   b. DW directions #0-4 no voluntary motion
   c. DW directions #5-9 continuous in-plane motion ("head shake" trajectory)
   d. DW directions #10-14 continuous through-plane motion ("nodding" trajectory)

TABLE 1 Sampling parameters of the diffusion tensor imaging scans

Parameters	DTI scan
TR	3000 ms
TE image\navigator echo	70\145 ms
FOV (R × P × S)	232 × 228 × 120 mm^3
Resolution image\navigator	1.0 × 1.0 × 4.0\5.0 × 5.0 × 4.0 mm^3
#slices N_z	30
Multi-band factor N_{MB}	3
CAIPI shift image\navigator	(FOV/3)\(FOV/2)
#interleaves N_i	4
In-plane reduction R_P image\navigator	4\1.6233
Partial Fourier factor image\navigator	0.632\1.000
Echo spacing image\navigator	1.3361\0.5829 ms
EPI factor* image/navigator	57\27
b-value	1,000 s/mm^2
#diffusion directions N_d	15
#T_2-weighted acquisitions	2
Scan time	3:30 min

*The EPI factor is given for the k-space sampling without partial Fourier reduction.

The subjects were asked to move at moderate rates of change to avoid the dominance of macroscopic intra-shot motion effects on the sensitive DWI sequence and provide sufficiently non-compromised data. Coil sensitivity maps were acquired once in advance using a gradient-echo prescan.[5] The EPI data preprocessing involves gridding the ramp samples in the readout direction and applying odd/even echo Nyquist ghost correction, based on EPI reference data jointly acquired for all SMS slices. The SMS phase from isocenter offsets in the slice direction was corrected for both the image and the navigator echo in advance.[41,42]

3.2 | Proposed algorithm: MoSaIC

The proposed navigated algorithm, termed motion-aware SMS-accelerated and interleaved image creation (MoSaIC) for DWI, is described in the following four sections: navigator reconstruction, navigator analysis, linear operator construction and full-volume image reconstruction. Figure 3 provides an overview of the reconstruction pipeline.

3.2.1 | Navigator reconstruction

The navigator data are upsampled to the high-resolution voxel size of the image echo using zero padding in k-space and a triangular apodization window to reduce Gibb's ringing. The navigators are reconstructed by *2D-SENSE*[43] with Tikhonov regularization (regularization parameter $\lambda_{nav} = 0.05$) recovering the unfolded slice groups of each shot (green box on the bottom left of Figure 3). Finally, residual slice-specific phases from RF excitation and blipped-CAIPI slice encoding are corrected.

3.2.2 | Navigator analysis

The navigator analysis contains a shot *phase extraction*, a *shot rejection* scheme and a *macroscopic motion* estimation. The *phase extraction* module obtains the phase maps $\boldsymbol{\varphi}_{s,l}$ of shot s and slice l of all diffusion-weighted shots from the low-resolution navigators.

Compromised shots are rejected using robust statistics on the $\ell 2$-norm of the diffusion-weighted navigator shot data. The *shot rejection* module uses the median absolute deviation (MAD) over all diffusion-weighted shot datasets and excludes shots whose $\ell 2$-norm drops below the threshold of $5 \cdot \text{MAD}$ from the median. The threshold was empirically set from analyzing the motion-corrupted navigators over

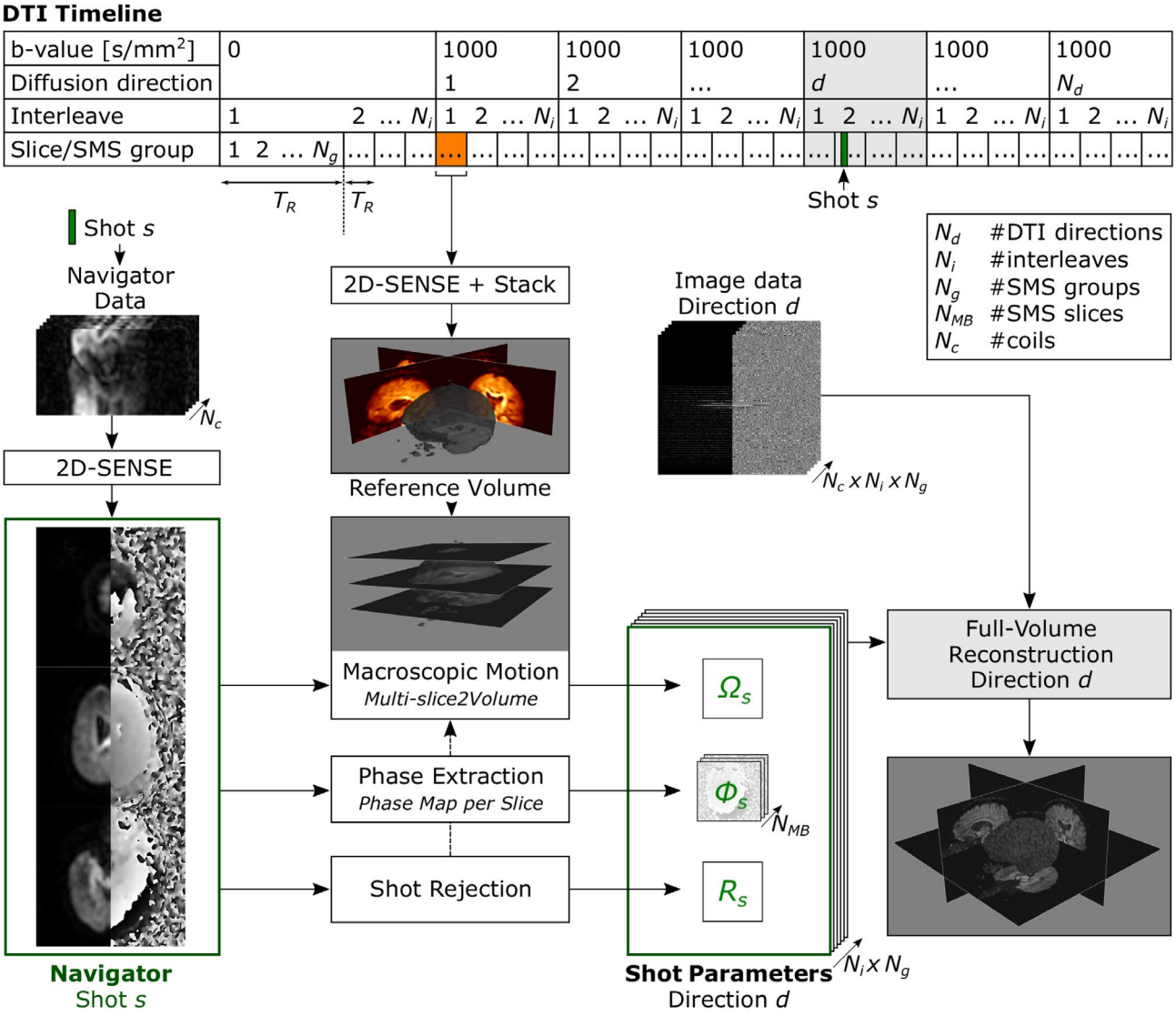

FIGURE 3 Overview of the proposed MoSaIC algorithm for a DTI acquisition. The DTI acquisition timeline loops over the diffusion-/T_2-weightings, the interleaves and the SMS groups (listed from outer to inner loops). All shot navigators are reconstructed by 2D-SENSE[43] (left green box) and the shot navigators from the reference TR (orange) are stacked to a full reference volume for registration. Next, the navigators are used to calculate shot rejection criteria, phase maps per shot and slice and macroscopic motion by multi-slice-to-volume registration. The full-volume reconstruction uses the shot-specific parameters (for Ω_s, Φ_s, R_s) to reconstruct motion-corrected high-resolution image volumes separately for each diffusion direction

multiple subjects and diffusion directions. Rejected shots are excluded from the registration strategy and from the full-volume reconstruction.

The *macroscopic motion* module estimates 3D rigid motion parameters using a shot-wise multi-slice-to-volume registration together with a motion detection strategy. The navigators are downsampled to roughly isotropic resolution of $(4\ \text{mm})^3$. The first full diffusion-weighted navigator volume (orange square in Figure 3) is used as the reference volume and is set as the moving image for the registration. This choice avoids resampling issues of the discrete SMS data.[54] The non-DWI data ($b = 0\ \text{s/mm}^2$) is assumed static and not registered in this work.

The multi-slice-to-volume registration was implemented in SimpleITK[55] with the following subtasks:

1. Volume-to-volume (Vol2Vol) registration of each full navigator volume per repetition time (TR)
   a. Method of moments pre-alignment
   b. Gradient descent-based registration
2. Motion detection per diffusion direction comparing TR-wise Vol2Vol parameters
3. SMS-to-volume (SMS2Vol) registration per shot (in acquisition order) if motion detected
   a. Linear interpolation of Vol2Vol parameters to shot time points

b. Warm start: choose Vol2Vol or previous SMS2Vol shot parameters by registration metric
c. Gradient descent-based registration
4. Median filter

The method of moments estimates rigid translations and rotations from the first and second statistical moments of the volumes. The registration uses the mutual information metric with 25 histogram bins, a 3D rigid versor transform and B-spline interpolation. The maximum number of iterations for gradient optimizations was 1000. For the Vol2Vol registration, the gradient descent uses a regular step size strategy with a minimum step of 10^{-6}.

The motion detection checks for each diffusion direction whether any rigid Vol2Vol parameter deviates more than 0.2 mm or 0.2 deg from the median among the N_i sub-volumes (TRs). This threshold was empirically set from accuracy analyses in registration simulations. If no motion is detected for a diffusion direction, the macroscopic motion operator is replaced by the identity operator I. Otherwise, the Vol2Vol preregistration parameters of the full TR volume are linearly interpolated to the shot time points. Then, a warm start strategy is employed that compares the registration metric for the interpolated Vol2Vol parameters and the SMS2Vol parameters of the previous shot. The subsequent gradient-based optimization is started from the preferred initial parameters and uses a line search strategy with at most 20 (line search) iterations. For SMS2Vol registration, the metric is evaluated only at SMS slice positions using a metric mask. Finally, a median filter (kernel size 5) is applied to each rigid motion parameter over time to ensure smoothness and to filter outliers.

3.2.3 | Linear operator construction

The macroscopic motion operator Ω for the high-resolution reconstruction is implemented as described by Cordero-Grande et al.[27] Translations use the Fourier shift theorem, whereas rotations are factored into three shears,[56] which are implemented via three 1D-FFTs. Moreover, the image $\boldsymbol{\rho}$ is reconstructed on an extended FOV to handle the fast Fourier transform (FFT)-related interpolation boundary conditions.

The operator Φ multiplies the sampled slices by the shot- and slice-specific navigator phase maps $\boldsymbol{\varphi}_{s,l}$. Moreover, encoding phases from the blipped-CAIPI image-space representation, off-isocenter encoding and slice-specific RF excitation phases φ_ℓ^{RF} are integrated into Φ, ensuring a continuous volume phase for the complex interpolation in Ω. The coil sensitivities in operator C are masked using a reference image and compressed[57] using a principal component analysis (PCA) with a threshold of 97% (resulting in 13 from initially 32 channels). The CAIPI operator Θ applies the integer-valued shifts in image space and adds up the SMS group. The EPI data are then masked in k_y-x-space according to the shot-specific EPI sampling trajectories by M^{trj}.

3.2.4 | Full-volume image reconstruction

The full-volume reconstruction is based on FGP.[53] The algorithm is initialized by the motion-unaware SMS-IRIS solution described below. Then, gradient updates and soft thresholding in the Daubechies 4 wavelet domain with transform T are iteratively performed. α was empirically set to 30. The FGP is stopped if either 100 iterations are exceeded or the normalized $\ell 2$-norm difference of two subsequent iterations δ_s[21] drops below 10^{-5}:

$$\delta_s = \frac{\left\|\boldsymbol{\rho}^{(k)} - \boldsymbol{\rho}^{(k-1)}\right\|_2^2}{\left\|\boldsymbol{\rho}^{(k-1)}\right\|_2^2}. \tag{3}$$

As the estimation of the Lipschitz constant for the FGP algorithm is demanding, a backtracking strategy was implemented.[53] The Lipschitz constant is initialized by the squared maximum absolute value of the coil sensitivity profiles. The Lipschitz constant is then increased by a factor of 1.5 if the objective function for the image estimate exceeds a quadratic approximation bound.[53]

3.3 | Reference algorithm: SMS-IRIS

The reference algorithm omits macroscopic motion during the image reconstruction. The static conditions, represented by an identity matrix I for the macroscopic motion operator $\Omega_s = I$, decouple the SMS slice group signals from each other and reduce the SENSE problem to small groups of aliasing pixels.

IRIS,[16] short for image reconstruction using image-space sampling function, is a SENSE formalism incorporating shot-to-shot phase variations from a navigator for interleaved single-slice EPI. In this work, we introduce a SMS extension, named SMS-IRIS, which requires adaption of IRIS to the interleaved phase encoding in k_z-k_y-space.[43] SMS-IRIS can also be interpreted as a SENSE-based formulation of the navigated method by Dai et al.[44] or as a navigated version of SMS-based MUSE.[45]

For SMS-IRIS, the shot- and slice-specific phase maps $\boldsymbol{\varphi}_{s,l}$ are estimated as described for MoSaIC. The non-iterative algorithm incorporates a weighted Tikhonov regularization $R(\boldsymbol{\rho}) = \|W\boldsymbol{\rho}\|_2^2$ with weighting matrix W ($N_\rho \times N_\rho$). W is constructed from the inverse absolute values of a motion-free T_2-weighted image filtered by a triangular window of about 4 mm isotropic k-space extent. $\alpha = 10^{-2}$ was set empirically. Moreover, the shot rejection is adopted to exclude severely

compromised shots. This navigated algorithm yields time-efficient reconstructions without macroscopic motion correction providing the MoSaIC initialization and a reference method in this work.

3.4 | Experimental design

The proposed algorithms were evaluated in simulation and in vivo studies. The static and motion-compromised in vivo data were reconstructed using SMS-IRIS and MoSaIC. Unsampled k-space portions from partial Fourier acquisitions are recovered by projections onto convex sets (POCS).[58] The algorithms were implemented in Python 3.6.9. Computations were performed on a cluster node with 48 GB RAM.

A tensor model was fit to the reconstructed images using Dipy[59] after affine registration, rotation correction of the diffusion directions and PCA-based DTI denoising.[60] The registration was performed in two subsequent steps using a rigid and an affine preregistration of the fast elastic image registration (FEIR) framework[61] with a normalized gradient field metric.[62] The first rigid alignment uses the FFT-based resampling[27] described above. The second affine alignment is resampled with the SimpleITK[55] B-Spline interpolation. The first T_2-weighted image of the static dataset was set as the registration reference. The diffusion direction per image volume (after the multi-shot reconstruction) was corrected for the estimated rotations from the average MoSaIC and the DTI alignment parameters.[29] The PCA thresholding τ-factor was set to the default value 2.3 and the SNR was estimated using Dipy's PCA noise estimation. Fractional anisotropy (FA) maps[1] and isotropic diffusion images[63] were calculated.

For the simulations, the motion-free SMS-IRIS reconstructions were used as ground truth data. Ten rigid motion trajectories were simulated by Gaussian processes for four motion scenarios, namely no, rigid in-plane, rigid through-plane and fully 3D rigid motion. The variances were set to $0.01\,\text{rad}^2$ and $0.5\,\text{mm}^2$. Diffusion phase maps were created by 3D second-order polynomials with random polynomial weights sampled according to Hu et al.[64] The sampling was adapted to the in vivo data with four-shot 3-SMS acquisition as well as FOV/3 and FOV/2 CAIPI shifts for image and navigator echo, respectively. The simulation data were created by selecting random diffusion directions from the ground truth data, applying the forward model and adding uncorrelated complex Gaussian noise in k-space, whereby the SNR was matched to the in vivo data.

The simulation data were recovered by SMS-IRIS and four MoSaIC variants to assess the registration components. All variants exclude rejected shots beforehand:

1. *MoSaIC Static*: No macroscopic motion correction ($\Omega_s = I$),
2. *MoSaIC Vol2Vol*: Rigid parameters from Vol2Vol registration,
3. *MoSaIC SMS2Vol*: Rigid parameters from Vol2Vol and subsequent SMS2Vol registration,
4. *MoSaIC* (default): Rigid parameters from Vol2Vol and subsequent SMS2Vol registration if motion was detected. Otherwise, the processing equals *MoSaIC static*.

The simulation results of all methods were registered to the ground truth by FEIR[61] with a rigid model, as the final volume registration of SMS-IRIS was considered standard DWI processing for a fair normalized root-mean-square error (nRMSE) comparison.

The simulation results were compared by the target registration error (TRE), nRMSE and reconstruction time. The TRE[65] evaluates the mean Euclidian distance over the registered coordinates u_r of target points r:

$$\text{TRE}\left(T_s', T_s^*\right) = \frac{\sum_{(s,r)\in\text{Target}} \left\| T_s'\left(u_r\right) - T_s^*\left(u_r\right) \right\|_2}{|\text{Target}|}, \qquad (4)$$

where T_s' is the estimated and T_s^* the true coordinate transformation of shot s. The target was defined as a mask derived from the ground truth by thresholding the absolute values at 5% of its maximum and selecting the SMS slices of each shot s. The cardinality $|\text{Target}|$ is the number of target points over all shots and slices (per diffusion direction).

4 | RESULTS

4.1 | Simulated DWI results

The DWI motion simulations provide a quantitative assessment of the registration and reconstruction performance. Figure 4 gives an overview of the simulation results for *SMS-IRIS* and the four *MoSaIC* variants. For all algorithms, TRE and nRMSE in Figures 4A,B increase with the degrees of freedom of the simulated motion profile. *MoSaIC Static* with wavelet denoising shows similar TRE and reduced nRMSE compared to *SMS-IRIS*. If motion is present, *SMS2Vol* outperforms *Vol2Vol* registration in terms of TRE and nRMSE, which itself improves on the static methods. *MoSaIC* provides similar results to *MoSaIC SMS2Vol*. For the static case, *SMS-IRIS, MoSaIC Static* and *MoSaIC* (with its motion detection) have a low TRE, which increases slightly from *MoSaIC Vol2Vol* to *SMS2Vol*. Figure 4C shows two transversal slice examples. For the first motion-free case, the results appear similar to the ground truth. The interhemispheric

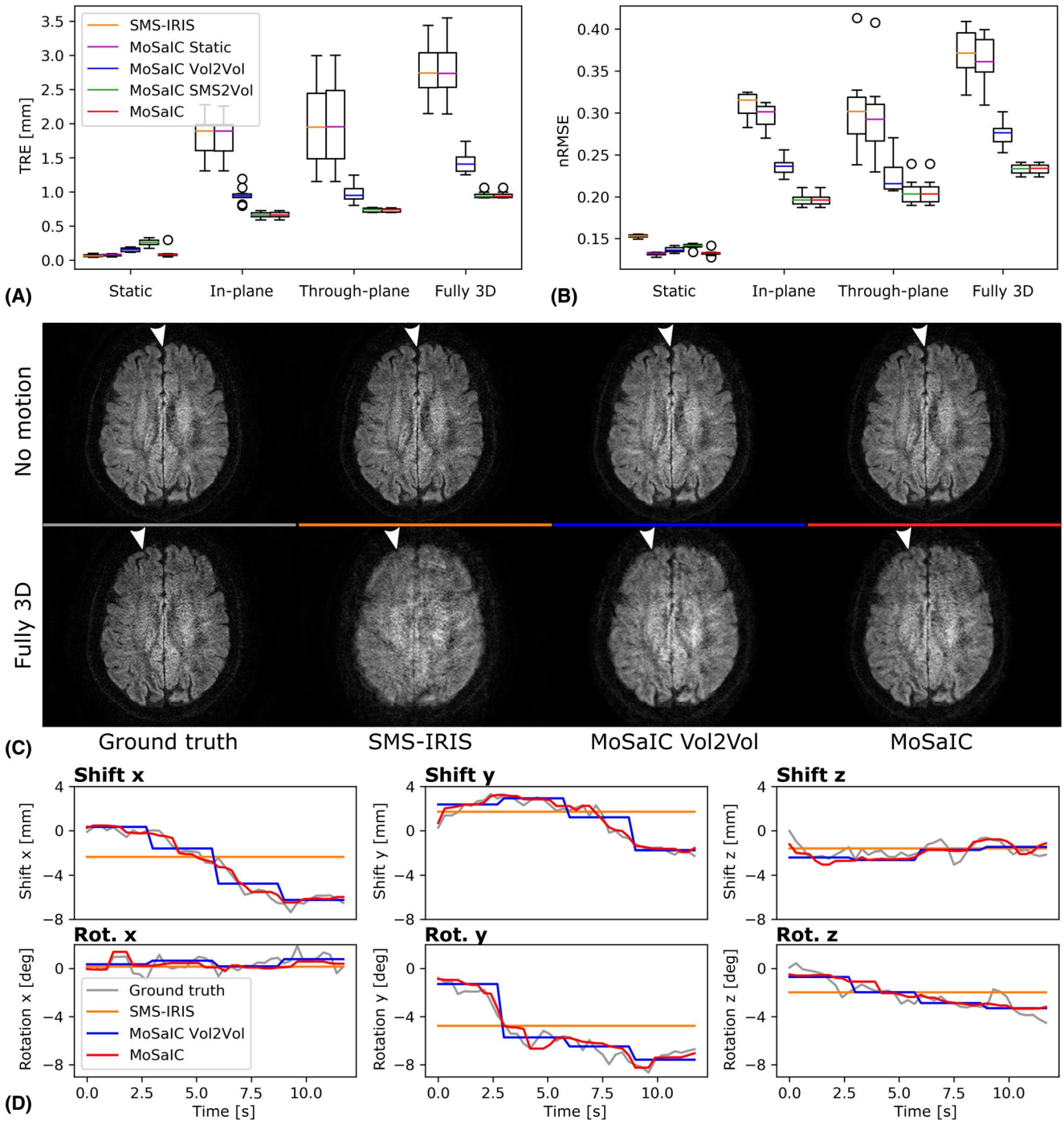

FIGURE 4 Full-volume reconstruction results of simulated four-shot 3-SMS data with random rigid trajectories and diffusion phases. Ten cases were simulated for different motion states, namely static, in-plane, through-plane and fully 3D rigid motion. A,B, The TRE and nRMSE, respectively, for SMS-IRIS and four MoSaIC variants as standard boxplots with whiskers of 1.5 times the interquartile range. C, Reconstruction examples without motion and with heavy fully 3D rigid motion are compared. D, Rigid motion estimates including the final full-volume registration to the reference (leading also to non-zero motion parameters for SMS-IRIS and MoSaIC static). Without motion, all methods provide results with similar visual appearance (arrows). If motion is present, MoSaIC with its SMS2Vol registration improves anatomical delineation (arrows) by taking into account sub-volume (sub-TR) shot-to-shot motion

fissure is well resolved for all methods. For the second 3D motion case, *SMS-IRIS* shows heavy blurring artifacts from inter-shot motion. *MoSaIC* is able to mitigate the motion artifacts and shows less blurring than *MoSaIC Vol2Vol*. The underlying motion estimates for the fully 3D rigid motion case are provided in Figure 4D.

The simulations show that the navigator with $5 \times 5 \times 4$ mm^3 resolution enables submillimeter TREs and improved

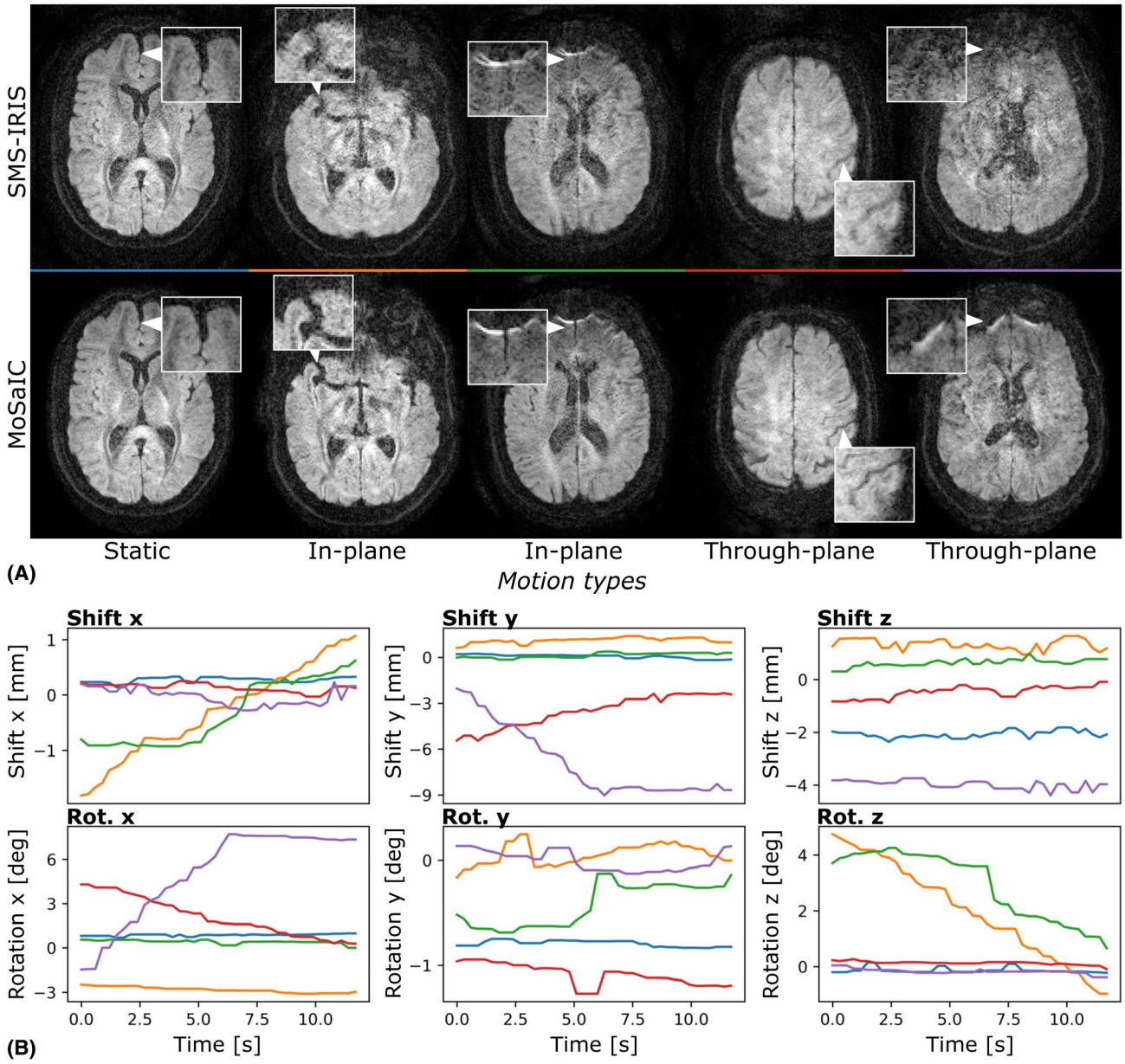

FIGURE 5 Segmented SMS image reconstructions without and with motion correction (in vivo data). A, Example slices of the full-volume reconstructions are shown for SMS-IRIS and MoSaIC, whereby different motion types have been present during the associated acquisitions. B, The estimated rigid trajectories of MoSaIC are plotted and associated to the images by a color code. MoSaIC provides similar image quality for the static dataset (blue) and mitigates macroscopic motion artifacts in the presence of both in-plane (orange and green) and through-plane (red and purple) motion (compare close-ups). The proposed motion detection was triggered for all cases

image quality of the high-resolution full-volume reconstructions. The achieved registration accuracy does not visibly differ between in- and through-plane motion (Figure 4A), although the nRMSE shows increased interquartile ranges for through-plane motion implying higher variation (Figure 4B). This could be related to the increased susceptibility to interpolation errors in the coarse slice direction. If motion is present, the high motion estimation resolution of SMS2Vol outperforms the Vol2Vol registration, which, in turn, improves on *SMS-IRIS*. Thus, the shot-to-shot motion estimation per SMS slice group captures continuous motion trajectories better, while having the same image reconstruction complexity as *MoSaIC Vol2Vol*. The rigid motion estimates in Figure 4D support this observation overall. Nevertheless, the motion parameters can contain temporary discrepancies above the sampling time resolution at some points, for example, for the y-rotation at approximately 5.0 s.

If no motion is present, the SMS2Vol registration (used for *MoSaIC SMS2Vol* and *MoSaIC*) is more instable and introduces higher errors, whereby the visual appearance is not visibly degraded (Figure 4C). *MoSaIC* uses the motion detection that switches off the SMS2Vol registration for small Vol2Vol estimates and thereby mitigates this downside by incorporating awareness of the achievable registration

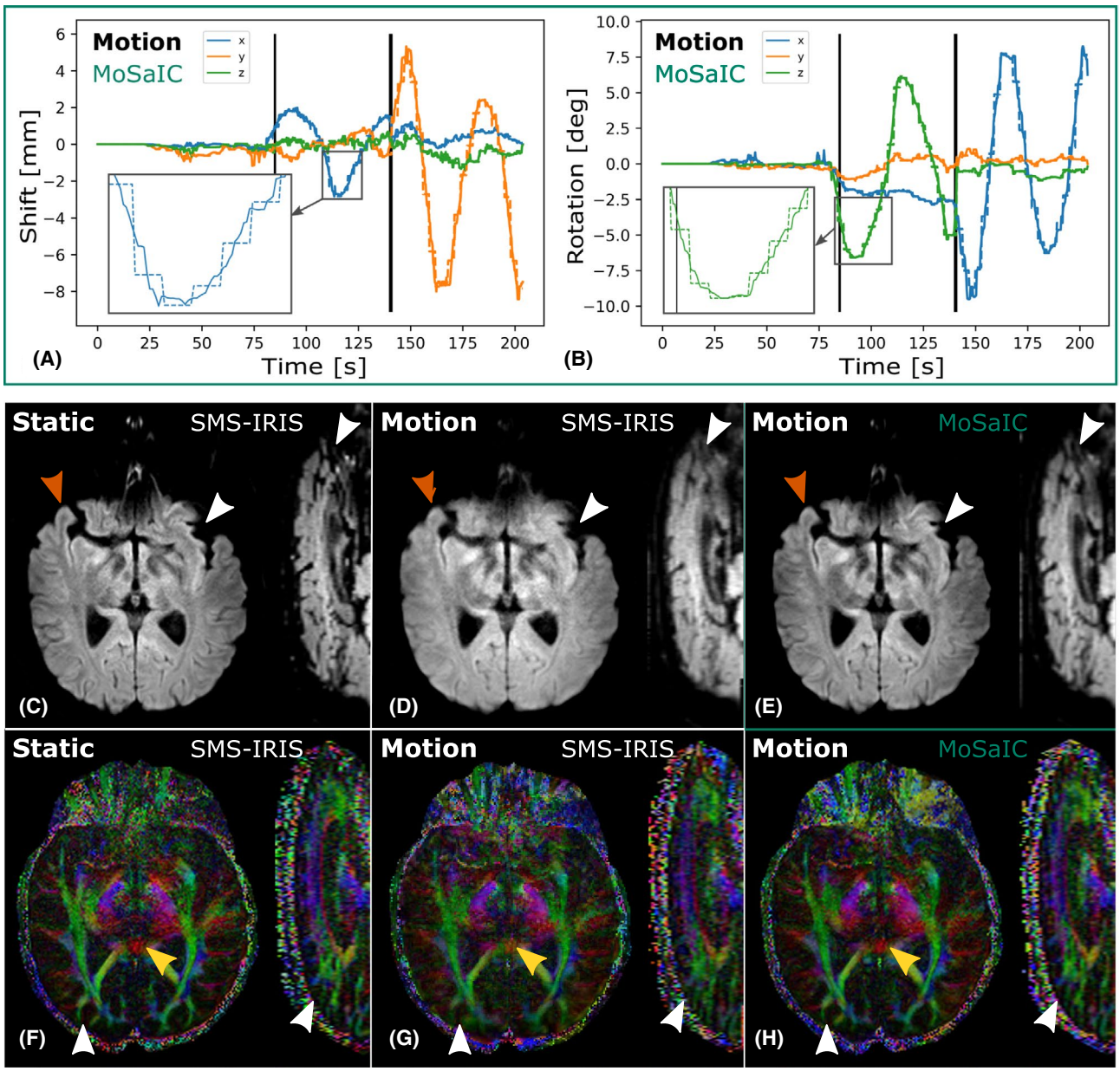

FIGURE 6 SMS-IRIS and MoSaIC reconstructions of in vivo DTI datasets measured under static and motion-disturbed conditions. A,B, The rigid shifts and rotations for the motion-disturbed dataset determined by MoSaIC are shown (mint green color code). The dashed lines with the same color in the background (see close-ups) provide the underlying Vol2Vol registration, whereas the black vertical lines indicate shots that were automatically rejected. Isotropic DWI images of SMS-IRIS are shown under static (C) and motion conditions (D), along with the MoSaIC reconstruction (E). F-H, Colored FA maps are displayed in the same order. MoSaIC recovers blurred structures (white arrows), improves the gray to white matter differentiation in the isotropic DWIs (orange arrows) and improves the directional fidelity in the colored FA maps (yellow arrows)

accuracy. The nRMSE improvement for through-plane motion demonstrates the benefits of the 3D motion correction over 2D in-plane motion correction.

4.2 | In vivo DWI results

An overview of the in vivo full-volume DWI reconstructions with different motion types is given in Figure 5. Reconstruction examples of *SMS-IRIS* and *MoSaIC* in Figure 5A are related to the associated rigid motion estimates of *MoSaIC* in Figure 5B by a color code. The images appear similar for the static case, whereas *MoSaIC* mitigates motion artifacts for the remaining cases (arrows). The motion detection was triggered for all datasets, whereby the SMS2Vol registration parameters remain almost constant for the supposedly static case (blue). Strong in-plane (z) rotations are detected for the orange and green datasets, leading to reduced blurring for *MoSaIC*. Light (red) and heavy (purple) nodding motion with rotations about the right-left axis (x) smear the

structures in the coarse through-plane direction for *SMS-IRIS*, which are reduced by *MoSaIC*. Despite the 3D rigid motion correction, residual artifacts remain for cases with heavy motion and the image quality of the static datasets might not be fully recoverable. For the motion datasets of the five subjects, the data rejection excluded [23, 9, 24, 0, 3] of 680 total shots, while [1, 1, 2, 0, 1] were rejected for the corresponding static datasets.

4.3 | In vivo DTI results

Figure 6 compares static and motion-disturbed DTI results for *SMS-IRIS* and *MoSaIC*. The estimated shift and rotation parameters of *MoSaIC* are displayed in Figure 6A,B, respectively, and rejected shots are indicated. The time resolution is $TR/N_g = 3/10\,\mathrm{s}$ with the number of SMS groups N_g yielding >3 Hz motion sampling frequency. For the static DTI dataset, the affine alignment resulted in 1.0042 ± 0.0047 and $-3 \cdot 10^{-5} \pm 0.0035$ for the non-rigid zoom and shear parameters, respectively.

The DTI analysis underlines the benefits of shot-to-shot motion correction for in vivo data. The static reconstructions comprise high SNR and clear delineation of the brain gyri and fractional anisotropies. The estimated motion trajectories reflect the motion study design, comprising roughly no motion in the first, in-plane in the second and through-plane motion in the last third. The shot rejection is active around 85 s and 140 s. Compared to *SMS-IRIS*, *MoSaIC* reduces blurring of motion-corrupted brain structures and improves the gray-to-white matter differentiation (orange arrows) as well as the directional accuracy of the tensor results (yellow arrows).

A quantitative histogram evaluation of the FAs and tensor traces between static and motion-corrupted reconstructions is presented for three subjects in Supporting Information Figure S2. The overlaps of the histograms from motion-corrupted datasets with the histograms from the static datasets are evaluated using the Kullback-Leibler divergence (KLD).[66] *MoSaIC* leads to a consistent, although for some cases modest, reduction of dissimilarity measured by the KLD.

The image quality improvements of *MoSaIC* come at the cost of higher computational complexity. The durations of the main processing steps are given in Table 2 for the DTI dataset in Figure 6. The highest computational cost of *MoSaIC* is placed by the FFT-based interpolation requiring multiple 1D-FFTs over the 3D data per shot and FGP iteration.

4.4 | Residual artifact evaluation

The *MoSaIC* reconstructions are affected by several remaining artifact types. Figure 7 compiles four types of artifacts (white arrows) that we encountered for *MoSaIC*. In all four cases, MoSaIC improves the blurring from head motion, but some artifacts remain, such as residual blurring of the interhemispheric fissure (Figure 7A), overlays of different susceptibility-induced deformations (Figure 7B), residual signal shadings (Figure 7C) and low SNR as well as speckled noise structures for strong motion cases (Figure 7D).

Another problem arises from the fact that some anatomies might remain unsampled if they have left the FOV, especially due to through-plane motion in feet-head direction. Nevertheless, the motion estimates give valuable information about the sampling locations, which can be translated to sampling densities in image space as outlined in Supporting Information Figure S3.

TABLE 2 Reconstruction times of main processing steps[a]

Processing step	Reference quantity	Total CPU Time [h:mm:ss]	KPI [s/cost driver]	
Navigator 2D-SENSE	All navigators	0:04:28	26.8	s/SMS group
Navigator Vol2Vol	All navigators	0:01:53	1.66	s/TR navigator volume
Navigator SMS2Vol	All navigators	0:55:26	4.89	s/shot
MoSaIC—3D rigid correction	DWI direction	6:11:11	317.02	s/FGP iteration
MoSaIC—no rigid correction	DWI direction	0:04:22	17.96	s/FGP iteration
SMS-IRIS	DWI direction	0:02:03	12.32	s/SMS group

[a]The numbers are given for a dataset containing 17 volumes (15 diffusion- + two T_2-weighted contrasts) with $256 \times 240 \times 30$ (R × P × S), multi-band 3, 10 SMS slice groups, four interleaves, and 32 coils. In addition to the total CPU times on an Intel Xeon Silver 4214 CPU @ 2.20GHz, the key performance indicators (KPIs) provide insights into the processing times per relevant cost driver indicating also potentials for parallelization. The MoSaIC durations are considered with 3D rigid correction and without ($\Omega_s = I$), depending on the motion detection switch.

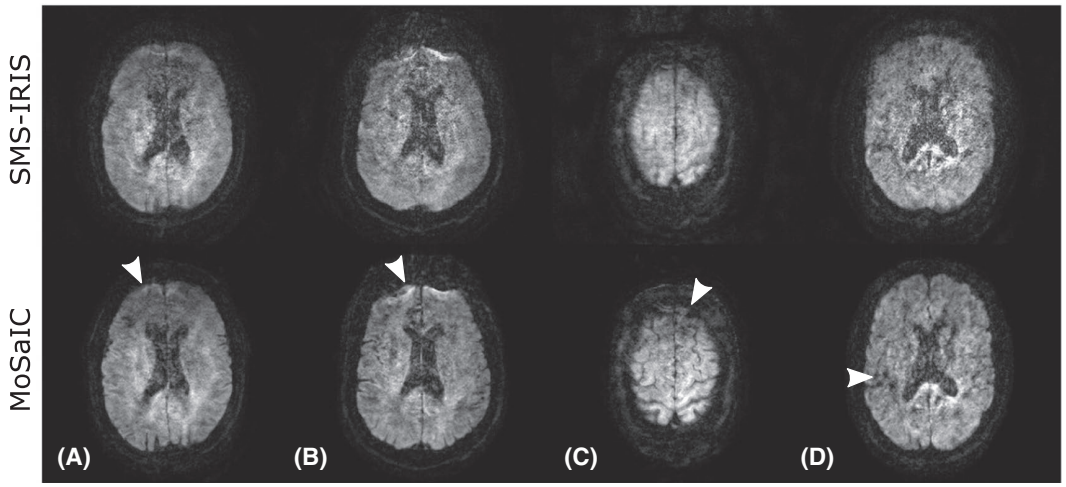

FIGURE 7 Examples of residual artifacts in MoSaIC reconstructions. MoSaIC mitigates macroscopic motion artifacts compared to SMS-IRIS, but some residual problems can remain. A, Blurring might remain if the registration accuracy is insufficient. B, Rotations cause shot-specific effects from off-resonances like susceptibility artifacts that are erroneously combined. C, Ghosting and slice leakage can result from residual shot-to-shot phase inconsistencies. D, Spoiled navigator diffusion phase estimates degrade the image quality

5 | DISCUSSION

MoSaIC provides 3D rigid motion-corrected full-volume reconstructions for navigated DWI with SMS and interleaved EPI sampling. The navigator shot images are employed to estimate the shot-specific phase variations, rigid motion states, and data rejection criteria. The multi-band excitation provides valuable data support in the slice direction enabling high temporal resolution through-plane motion evaluation. The performance of MoSaIC was evaluated in simulations and in vivo for DTI scans with 4 shots and $N_{MB} = 3$ yielding shot motion estimates at roughly 3 Hz temporal resolution.

5.1 | Unmodeled shot variations

Several unmodeled shot variations[2] spoil the shot similarity for image registration and multi-shot image reconstructions. First, local off-resonance effects manifest as geometric distortions in phase encoding direction for EPI. As head rotations vary the effective phase encoding direction, the local distortions differ per shot (Figure 7B). Geometric distortions can be reduced by readout-segmented acquisitions[14,15] or corrected by model extensions accounting for off-resonance effects using B_0 map estimates.[67] This improves the shot navigator similarity for registration and offers higher local shot consistency for multi-shot reconstructions. In the current setting, the distortions also introduce mismatches between the EPI data and the gradient-echo sensitivity pre-scan, which could be avoided estimating the sensitivities from the non-DWI EPI data using ESPIRiT.[68]

Second, field inhomogeneities can introduce slice-specific gradient timing offsets that are not captured by the current pre-scan and introduce Nyquist ghosting. The slice-adaptive odd-even corrections could, for example, be addressed by model-based estimation.[69]

Third, eddy currents especially from the strong diffusion-sensitizing gradients induce generally affine transformations and exceed rigid modeling. Although the zoom and shear parameters were rather small in this study, they depend on the sequence and the system tuning. The field deviations can be reduced by twice-refocused sequences[12] or corrected by model-based reconstructions.[3] Alternatively, the motion model could be extended to affine transformations.

Fourth, the effective diffusion direction is affected by subject rotations leading to shot-wise diffusion contrast variations.[31] The presented framework assumes for each diffusion direction that the induced contrast variations are negligible under sufficiently small rotations. Contrast corrections can be introduced by imposing q-space relations[2,31,70] between the shots.

5.2 | Navigator analysis

Navigation strategies are prone to potential signal differences between the image and the navigator data. Intra-shot motion might spoil the acquisition windows differently, affect the navigator refocusing and lead to a geometric mismatch.[24] A central assumption of the current multi-shot model is that the object comprises one consistent phase map, whose shot variations are completely described by the navigator phase and the encoding model. Residual phase inconsistencies and noise from intra-shot motion impede proper pixel unfolding in the full-volume image reconstruction, which can lead to ghosting (Figure 7C) and speckled noise (Figure 7D) artifacts.

Self-navigation is currently intractable for the studied macroscopic motion-disturbed data due to the large g-factor penalty. The lack of viable shot reference data from the image echo impedes the evaluation of intra-shot motion leaving this as an open issue for further studies. The resolution of the single-shot navigator introduces another signal discrepancy for phase and macroscopic motion estimation.

The SMS-to-volume registration is itself a challenging problem[54] that requires careful design of the parameter initialization and gradient optimization. Regarding the warm start strategy, the exploitation of time correlations in combination with the challenging optimization landscape can cause temporal discrepancies of the registration parameters as described in the last section for Figure 4. The registration accuracy is further impeded by the low SNR of DWI, the coarse navigator resolution, intra-shot motion and the unmodeled shot-specific variations. Thus, MoSaIC might nevertheless suffer from residual blurring artifacts (Figure 7A). In addition, motion for T_2-weighted data ($b = 0$ s/mm^2) could be included by registrations to the first T_2-weighted navigator volume. Conversely, inter-contrast registrations between diffusion- and T_2-weighted data remained unstable.

5.3 | Full-volume image reconstruction

The encoding model mainly determines the quality of the shot navigators and the full-volume image reconstructions comprising the k-space sampling trajectory and the sensitivity encoding. Therefore, the deployment of other potentially non-Cartesian trajectories and improved coil setups might be beneficial.[6] As part of the sampling trajectory, this also applies to optimizations of the navigator CAIPI shift, which is set to FOV/2 in this work.

MoSaIC solves the multi-shot problem with $\ell 1$-norm regularization by fast gradient projections, and the sparsity-enforcing regularization was shown to reduce the nRMSE in simulations. With an $\ell 2$-norm regularization, the multi-shot problem is tractable by the conjugate gradients method,[66] whereby both methods require one application of the forward model and its adjoint per iteration.

The choice of interpolation is a crucial trade-off balancing image quality and computational cost. The macroscopic motion operator Ω resamples the image volume for all shots, twice per FGP iteration. GPU-based implementations[27] can significantly accelerate this processing. Furthermore, the motion detection of MoSaIC analyses the volumetric preregistration parameters for significant variations and allows circumventing the expensive image resampling.

MoSaIC is currently restricted to anisotropic resolution with coarse slice thickness, which might be overcome by improved slice encoding schemes. The reduction of the slice thickness quickly becomes SNR-critical for the proposed acquisition and requires enhanced slice encoding, such as simultaneous 3D multi-slab approaches[46] or improved radiofrequency slice encoding.[71] The use of thinner slices should ease the relative interpolation burden, but, at the same time, thinner slices are affected more severely by motion.

5.4 | Informed sampling and reconstruction

MoSaIC uses a rather simple shot rejection analyzing the navigators' energy content similar to Ref. 11. More elaborate criteria to detect degenerate signals involve correlation measures[17] or k-space signal moments.[15] The reacquisition of deteriorated signals[15] presents a valuable extension to exclude malicious data without sacrificing SNR. Through the 3D rigid motion estimation, MoSaIC is furthermore aware of the spatial sampling density making reacquisitions of undersampled areas in image-space feasible as discussed for Supporting Information Figure S3.

Prospective methods[36] represent an important alternative for macroscopic motion corrections. Prospective control allows also for affine online corrections of the gradient coordinate system mitigating the motion artifacts directly in the acquisition and thereby facilitates the computational burden. The online adaption of the diffusion gradient[35] and phase encoding direction also reduce shot contrast and distortion variations. Conversely, they depend on the functionality of the external system and cannot account for local motion transformations and phase variations.[36] In synergistic use, prospective methods could improve the database and ease the interpolation by reducing the residual motion, while retrospective corrections cover remaining artifacts to enable highly motion-robust DWI.

6 | CONCLUSIONS

The proposed MoSaIC framework improves diffusion-weighted imaging quality in the presence of head motion. The use of navigation and SMS acquisitions enable 3D rigid registration for motion-corrected volume reconstructions, which was presented for four-shot, 3-SMS DTI. The presented algorithms make combined use of SMS and interleaving allowing flexible balancing of SNR and scan time. This model-based strategy offers potentials for smart motion-aware image sampling and reconstruction to improve the robustness of DWI in clinical practice.

ACKNOWLEDGMENTS

Open Access funding enabled and organized by Projekt DEAL.

CONFLICT OF INTEREST

Peter Börnert is a Philips employee. The associated research project of Malte Riedel was financed by Philips as indicated in the Funding Information.

ORCID

Malte Riedel (né Steinhoff) https://orcid.org/0000-0002-5703-7408

REFERENCES

1. Le Bihan D, Mangin J-F, Poupon C, et al. Diffusion tensor imaging: concepts and applications. *JMRI*. 2001;13:534-546.
2. Wu W, Miller KL. Image formation in diffusion MRI: a review of recent technical developments: review of image formation in dMRI. *JMRI*. 2017;46:646-662.
3. Fessler J. Model-based image reconstruction for MRI. *IEEE Signal Process Mag*. 2010;27:81-89.
4. Roemer PB, Edelstein WA, Hayes CE, Souza SP, Mueller OM. The NMR phased array. *Magn Reson Med*. 1990;16:192-225.
5. Pruessmann KP, Weiger M, Scheidegger MB, Boesiger P. SENSE: sensitivity encoding for fast MRI. *Magn Reson Med*. 1999;42:952-962.
6. Pruessmann KP, Weiger M, Börnert P, Boesiger P. Advances in sensitivity encoding with arbitrary k-space trajectories. *Magn Reson Med*. 2001;46:638-651.
7. Griswold MA, Jakob PM, Heidemann RM, et al. Generalized autocalibrating partially parallel acquisitions (GRAPPA). *Magn Reson Med*. 2002;47:1202-1210.
8. McKinnon GC. Ultrafast interleaved gradient-echo-planar imaging on a standard scanner. *Magn Reson Med*. 1993;30:609-616.
9. Anderson AW, Gore JC. Analysis and correction of motion artifacts in diffusion weighted imaging. *Magn Reson Med*. 1994;32:379-387.
10. Miller KL, Pauly JM. Nonlinear phase correction for navigated diffusion imaging. *Magn Reson Med*. 2003;50:343-353.
11. Butts K, Pauly J, De Crespigny A, Moseley M. Isotropic diffusion-weighted and spiral-navigated interleaved EPI for routine imaging of acute stroke. *Magn Reson Med*. 1997;38:741-749.
12. Atkinson D, Porter DA, Hill DLG, Calamante F, Connelly A. Sampling and reconstruction effects due to motion in diffusion-weighted interleaved echo planar imaging. *Magn Reson Med*. 2000;44:101-109.
13. Atkinson D, Counsell S, Hajnal JV, Batchelor PG, Hill DL, Larkman DJ. Nonlinear phase correction of navigated multi-coil diffusion images. *Magn Reson Med*. 2006;56:1135-1139.
14. Holdsworth SJ, Skare S, Newbould RD, Guzmann R, Blevins NH, Bammer R. Readout-segmented EPI for rapid high resolution diffusion imaging at 3T. *Eur J Radiol*. 2008;65:36-46.
15. Porter DA, Heidemann RM. High resolution diffusion-weighted imaging using readout-segmented echo-planar imaging, parallel imaging and a two-dimensional navigator-based reacquisition. *Magn Reson Med*. 2009;62:468-475.
16. Jeong H-K, Gore JC, Anderson AW. High-resolution human diffusion tensor imaging using 2-D navigated multishot SENSE EPI at 7 T. *Magn Reson Med*. 2013;69:793-802.
17. Pipe JG, Farthing VG, Forbes KP. Multishot diffusion-weighted FSE using PROPELLER MRI. *Magn Reson Med*. 2002;47:42-52.
18. Liu C, Moseley ME, Bammer R. Simultaneous phase correction and SENSE reconstruction for navigated multi-shot DWI with non-cartesian k-space sampling. *Magn Reson Med*. 2005;54:1412-1422.
19. Chen N, Guidon A, Chang H-C, Song AW. A robust multi-shot scan strategy for high-resolution diffusion weighted MRI enabled by multiplexed sensitivity-encoding (MUSE). *Neuroimage*. 2013;72:41-47.
20. Chu M-L, Chang H-C, Chung H-W, Truong T-K, Bashir MR, Chen N. POCS-based reconstruction of multiplexed sensitivity encoded MRI (POCSMUSE): a general algorithm for reducing motion-related artifacts: POCSMUSE reconstruction for motion artifact removal. *Magn Reson Med*. 2015;74:1336-1348.
21. Guo H, Ma X, Zhang Z, Zhang B, Yuan C, Huang F. POCS-enhanced inherent correction of motion-induced phase errors (POCS-ICE) for high-resolution multishot diffusion MRI: high resolution multishot DWI without navigator. *Magn Reson Med*. 2016;75:169-180.
22. Mani M, Jacob M, Kelley D, Magnotta V. Multi-shot sensitivity-encoded diffusion data recovery using structured low-rank matrix completion (MUSSELS): annihilating filter K-space formulation for multi-shot DWI recovery. *Magn Reson Med*. 2017;78:494-507.
23. Hu Y, Levine EG, Tian Q, et al. Motion-robust reconstruction of multishot diffusion-weighted images without phase estimation through locally low-rank regularization. *Magn Reson Med*. 2019;81:1181-1190.
24. Zaitsev M, Maclaren J, Herbst M. Motion artifacts in MRI: a complex problem with many partial solutions: motion artifacts and correction. *JMRI*. 2015;42:887-901.
25. Batchelor PG, Atkinson D, Irarrazaval P, Hill DLG, Hajnal J, Larkman D. Matrix description of general motion correction applied to multishot images. *Magn Reson Med*. 2005;54:1273-1280.
26. Bammer R, Aksoy M, Liu C. Augmented generalized SENSE reconstruction to correct for rigid body motion. *Magn Reson Med*. 2007;57:90-102.
27. Cordero-Grande L, Teixeira RPAG, Hughes EJ, Hutter J, Price AN, Hajnal JV. Sensitivity encoding for aligned multishot magnetic resonance reconstruction. *IEEE Trans Comput Imaging*. 2016;2:266-280.
28. Cordero-Grande L, Hughes EJ, Hutter J, Price AN, Hajnal JV. Three-dimensional motion corrected sensitivity encoding reconstruction for multi-shot multi-slice MRI: application to neonatal brain imaging: aligned multi-shot multi-slice MRI. *Magn Reson Med*. 2017;79:1365-1376.
29. Dong Z, Wang F, Ma X, Dai E, Zhang Z, Guo H. Motion-corrected k-space reconstruction for interleaved EPI diffusion imaging: motion correction for iEPI DWI. *Magn Reson Med*. 2018;79:1992-2002.
30. Steinhoff M, Mertins A, Börnert P. SENSE-based Multi-shot DWI reconstruction with extra-navigated rigid motion and contrast correction for brain EPI. In: Proceedings of the 2020 ISMRM & SMRT Virtual Conference & Exhibition. 2020:Program no. 4339. https://index.mirasmart.com/ISMRM2020/PDFfiles/4339.html.
31. Guhaniyogi S, Chu M-L, Chang H-C, Song AW, Chen N. Motion immune diffusion imaging using augmented MUSE for high-resolution multi-shot EPI: motion immune diffusion imaging using AMUSE. *Magn Reson Med*. 2016;75:639-652.
32. Steinhoff M, Nehrke K, Mertins A, Börnert P. Segmented diffusion imaging with iterative motion-corrected reconstruction (SEDIMENT) for brain echo-planar imaging. *NMR Biomed*. 2020:33;e4185. http://dx.doi.org/10.1002/nbm.4185.
33. Thesen S, Heid O, Mueller E, Schad L. Prospective acquisition correction for head motion with image-based tracking for real-time fMRI. *Magn Reson Med*. 2000;44:457-465.
34. Zaitsev M, Dold C, Sakas G, Hennig J, Speck O. Magnetic resonance imaging of freely moving objects: prospective real-time motion correction using an external optical motion tracking system. *Neuroimage*. 2006;31:1038-1050.

35. Herbst M, Maclaren J, Weigel M, Korvink J, Hennig J, Zaitsev M. Prospective motion correction with continuous gradient updates in diffusion weighted imaging: prospective motion correction with continuous gradient updates. *Magn Reson Med*. 2012;67:326-338.
36. Maclaren J, Herbst M, Speck O, Zaitsev M. Prospective motion correction in brain imaging: a review. *Magn Reson Med*. 2013;69:621-636.
37. Herbst M, Zahneisen B, Knowles B, Zaitsev M, Ernst T. Prospective motion correction of segmented diffusion weighted EPI: prospective motion correction of segmented diffusion weighted EPI. *Magn Reson Med*. 2015;74:1675-1681.
38. Barth M, Breuer F, Koopmans PJ, Norris DG, Poser BA. Simultaneous multislice (SMS) imaging techniques: SMS imaging. *Magn Reson Med*. 2016;75:63-81.
39. Breuer FA, Blaimer M, Heidemann RM, Mueller MF, Griswold MA, Jakob PM. Controlled aliasing in parallel imaging results in higher acceleration (CAIPIRINHA) for multi-slice imaging. *Magn Reson Med*. 2005;53:684-691.
40. Breuer FA, Blaimer M, Mueller MF, et al. Controlled aliasing in volumetric parallel imaging (2D CAIPIRINHA). *Magn Reson Med*. 2006;55:549-556.
41. Setsompop K, Gagoski BA, Polimeni JR, Witzel T, Wedeen VJ, Wald LL. Blipped-controlled aliasing in parallel imaging for simultaneous multislice echo planar imaging with reduced g-factor penalty. *Magn Reson Med*. 2012;67:1210-1224.
42. Zahneisen B, Poser BA, Ernst T, Stenger VA. Three-dimensional Fourier encoding of simultaneously excited slices: generalized acquisition and reconstruction framework: 3D Fourier encoding for SMS acquisitions. *Magn Reson Med*. 2014;71:2071-2081.
43. Zahneisen B, Ernst T, Poser BA. SENSE and simultaneous multislice imaging: SENSE and simultaneous multislice imaging. *Magn Reson Med*. 2015;74:1356-1362.
44. Dai E, Ma X, Zhang Z, Yuan C, Guo H. Simultaneous multislice accelerated interleaved EPI DWI using generalized blipped-CAIPI acquisition and 3D K-space reconstruction: SMS Accelerated iEPI DWI. *Magn Reson Med*. 2017;77:1593-1605.
45. Chang H-C, Guhaniyogi S, Chen N. Interleaved diffusion-weighted improved by adaptive partial-Fourier and multiband multiplexed sensitivity-encoding reconstruction: reconstruction framework for artifact-free DWI. *Magn Reson Med*. 2015;73:1872-1884.
46. Moeller S, Ramanna S, Lenglet C, et al. Self-navigation for 3D multishot EPI with data-reference. *Magn Reson Med*. 2020;84:1747-1762.
47. Mani M, Jacob M, McKinnon G, et al. SMS MUSSELS: a navigator-free reconstruction for simultaneous multi-slice-accelerated multi-shot diffusion weighted imaging. *Magn Reson Med*. 2020;83:154-169.
48. Herbst M, Poser BA, Singh A, et al. Motion correction for diffusion weighted SMS imaging. *Magn Reson Med*. 2017;38:33-38.
49. Teruel JR, Kuperman JM, Dale AM, White NS. High temporal resolution motion estimation using a self-navigated simultaneous multi-slice echo planar imaging acquisition: motion estimation using self-navigated SMS-EPI acquisition. *J Magn Reson Imaging*. 2018;48:780-787.
50. Hoinkiss DC, Erhard P, Breutigam N-J, von Samson-Himmelstjerna F, Günther M, Porter DA. Prospective motion correction in functional MRI using simultaneous multislice imaging and multislice-to-volume image registration. *Neuroimage*. 2019;200:159-173.
51. Marami B, Scherrer B, Khan S, et al. Motion-robust diffusion compartment imaging using simultaneous multi-slice acquisition. *Magn Reson Med*. 2019;81:3314-3329.
52. Lustig M, Donoho D, Pauly JM. Sparse MRI: the application of compressed sensing for rapid MR imaging. *Magn Reson Med*. 2007;58:1182-1195.
53. Beck A, Teboulle M. A fast iterative shrinkage-thresholding algorithm for linear inverse problems. *SIAM J Imaging Sci*. 2009;2:183-202.
54. Ferrante E, Paragios N. Slice-to-volume medical image registration: a survey. *Med Image Anal*. 2017;39:101-123.
55. Beare R, Lowekamp B, Yaniv Z. Image segmentation, registration and characterization in R with SimpleITK. *J Stat Softw*. 2018;86. http://dx.doi.org/10.18637/jss.v086.i08.
56. Unser M, Thevenaz P, Yaroslavsky L. Convolution-based interpolation for fast, high-quality rotation of images. *IEEE Trans Image Process*. 1995;4:1371-1381.
57. Buehrer M, Pruessmann KP, Boesiger P, Kozerke S. Array compression for MRI with large coil arrays. *Magn Reson Med*. 2007;57:1131-1139.
58. Liang Z-P, Lauterbur PC. *Principles of Magnetic Resonance Imaging: A Signal Processing Perspective*. Washington, DC: SPIE Optical Engineering Press; 2000.
59. Garyfallidis E, Brett M, Amirbekian B, et al. Dipy, a library for the analysis of diffusion MRI data. *Front Neuroinform*. 2014;8:8.
60. Manjón JV, Coupé P, Concha L, Buades A, Collins DL, Robles M. Diffusion weighted image denoising using overcomplete local PCA. Gong G, ed. *PLoS One*. 2013;8:e73021.
61. Kabus S, Lorenz C. Fast elastic image registration. *Medical Image Analysis for the Clinic: A Grand Challenge*. 2010;89:81-89.
62. Haber E, Modersitzki J. Beyond mutual information: a simple and robust alternative. In: Meinzer H-P, Handels H, Horsch A, Tolxdorff T, ed. *Bildverarbeitung Für Die Medizin 2005*. Berlin/Heidelberg: Springer-Verlag; 2005:350-354.
63. Mukherjee P, Berman JI, Chung SW, Hess CP, Henry RG. Diffusion tensor MR imaging and fiber tractography: theoretic underpinnings. *Am J Neuroradiol*. 2008;29:632-641.
64. Hu Z, Ma X, Truong T-K, Song AW, Guo H. Phase-updated regularized SENSE for navigator-free multishot diffusion imaging: PR-SENSE for DWI. *Magn Reson Med*. 2017;78:172-181.
65. Kuklisova-Murgasova M, Quaghebeur G, Rutherford MA, Hajnal JV, Schnabel JA. Reconstruction of fetal brain MRI with intensity matching and complete outlier removal. *Med Image Anal*. 2012;16:1550-1564.
66. Vogel CR. *Computational Methods for Inverse Problems*. Philadelphia, PA: Society for Industrial and Applied Mathematics; 2002.
67. Andersson JLR, Skare S, Ashburner J. How to correct susceptibility distortions in spin-echo echo-planar images: application to diffusion tensor imaging. *Neuroimage*. 2003;20:870-888.
68. Uecker M, Lai P, Murphy MJ, et al. ESPIRiT-an eigenvalue approach to autocalibrating parallel MRI: where SENSE meets GRAPPA. *Magn Reson Med*. 2014;71:990-1001.
69. Hoge WS, Setsompop K, Polimeni JR. Dual-polarity slice-GRAPPA for concurrent ghost correction and slice separation in simultaneous multi-slice EPI. *Magn Reson Med*. 2018;80:1364-1375.
70. Hu Y, Wang X, Tian Q, et al. Multi-shot diffusion-weighted MRI reconstruction with magnitude-based spatial-angular locally low-rank regularization (SPA-LLR). *Magn Reson Med*. 2020;83:1596-1607.

71. Setsompop K, Fan Q, Stockmann J, et al. High-resolution in vivo diffusion imaging of the human brain with generalized slice dithered enhanced resolution: simultaneous multislice (gSlider-SMS): high-resolution diffusion imaging with gSlider-SMS. *Magn Reson Med*. 2018;79:141-151.

SUPPORTING INFORMATION

Additional Supporting Information may be found online in the Supporting Information section.

FIGURE S1 Schematic Stejskal-Tanner spin-echo sequence diagram for navigated multi-shot DWI with SMS extension. The sequence uses multi-band radio frequency (RF) excitation (MB 90°) and refocusing (MB 180°) pulses to form the image and navigator echo for SMS acquisition. The dotted lines indicate the diffusion-sensitizing gradients. In-plane accelerations are achieved using interleaved EPI for the image echo and single-shot EPI with moderate regular undersampling for the navigator echo. Slice gradient blips are added for blipped-CAIPI encoding with slice-specific shifts, which significantly improve the coil encoding capabilities. The image echo is sampled with a FOV/3 shift between adjacent slices, while the navigator slices are shifted by FOV/2

FIGURE S2 Quantitative histogram comparisons of SMS-IRIS and MoSaIC results between static and motion-disturbed datasets for three subjects. The histograms were created with 100 bins producing bin widths of 0.01 for the FA maps and $9 \cdot 10^{-5}$ s/mm^2 for the traces. (A): Fractional anisotropy (upper row) and trace (bottom row) histograms are shown for three subjects (columns). The static SMS-IRIS (green) results are compared to SMS-IRIS (orange) and MoSaIC (blue) under motion conditions. The MoSaIC histograms for motion datasets (blue) are overall closer to SMS-IRIS for static datasets (green) than the SMS-IRIS histograms for motion datasets (orange). However, MoSaIC still shows significant differences to the static cases. Please note that the comparison involves a resampling of the motion datasets from their specific reconstruction grids and a direct comparison is not trivial. (B): Histogram overlap evaluations of the motion cases to the associated static cases by the Kullback-Leibler divergence (KLD). The histogram distances of MoSaIC, measured by the KLD, decrease for all subjects compared to SMS-IRIS

FIGURE S3 Image-space sampling density estimation by Voronoi partitions for regular SMS EPI under shot-specific motion. For the presented dataset, SMS-IRIS shows strong motion-induced blurring from both in- and through-plane rotations, which is resolved by MoSaIC. Nevertheless, the SNR falls off towards the right occipital lobe. The motion-aware sampling density counts the number of samples that fall into a given voxel according to the rigid motion estimates. The result can be smoothened by a Gaussian in-plane kernel ($\sigma = 2$). Therefore, the numbers on the filtered sampling density plot indicate, how often a particular area in the image domain has been sampled in presence of motion. The analysis indicates that the affected area remained unsampled (below red line), as it left the FOV due to nodding-type head motion. The sampling density provides beneficial information, which could be used for dedicated reacquisition strategies or to tag low SNR regions

How to cite this article: Riedel (né Steinhoff) M, Setsompop K, Mertins A, Börnert P. Segmented simultaneous multi-slice diffusion-weighted imaging with navigated 3D rigid motion correction. *Magn Reson Med*. 2021;86:1701–1717. https://doi.org/10.1002/mrm.28813